72nd International Astronautical Congress (IAC), Dubai, United Arab Emirates, 25-29 October 2021.

IAC-21-C1.7.8

Keplerian map theory for high-fidelity prediction of the third-body perturbative effect

Giudici L.[a]*, Colombo C.[a]

[a] *Department of Aerospace Science and Technology, Politecnico di Milano, Via La Masa 34, Milano 20156*, lorenzo1.giudici@polimi.it, camilla.colombo@polimi.it
* Corresponding Author

Abstract

This paper introduces an accurate model to monitor the motion of a particle of negligible mass under the simultaneous gravitational attraction of many celestial bodies, in the restricted three-body problem dynamical regime. It relies on the Lagrange planetary equations and applies the perturbation approach to the three-body potential. This approach benefits from a dynamical model based on the slow-varying Keplerian elements, with respect to the classical formulation of the N-body problem in Cartesian coordinates, which ensures a high computational efficiency. An extensive validation of the theory is presented, to test the accuracy of the model in different scenarios and prove its competitiveness from a computational point of view. The model is eventually adopted for computing a trajectory where the third-body perturbation plays a significant role; the target mission is a multi-flyby trajectory design in the Jupiter sphere of influence, where the gravity fields of the gaseous planet and the four Galilean moons are simultaneously considered.

Keywords: Keplerian map, three-body problem, perturbations, trajectory optimisation, multi-flyby trajectory

Nomenclature

a	=	semi-major axis of the mass-less particle
e	=	eccentricity of the mass-less particle
i	=	inclination of the mass-less particle
Ω	=	right ascension of ascending node of the mass-less particle
ω	=	argument of periapsis of the mass-less particle
ν	=	true anomaly of the mass-less particle
E	=	eccentric anomaly of the mass-less particle
a_{3B}	=	semi-major axis of the disturbing body
e_{3B}	=	eccentricity of the disturbing body
i_{3B}	=	inclination of the disturbing body
Ω_{3B}	=	right ascension of ascending node of the disturbing body
ω_{3B}	=	argument of periapsis of the disturbing body
ν_{3B}	=	true anomaly of the disturbing body
R	=	Disturbing function of the third-body perturbation

Acronyms/Abbreviations

CRTBP	=	Circular Restricted Three-Body Problem
SOI	=	Sphere Of Influence
NEO	=	Near-Earth Object
JUICE	=	JUpiter ICy moons Explorer
DSM	=	Deep Space Manoeuvre
TOF	=	Time Of Flight

1. Introduction

Since the very beginning of space exploration, the modelling of the simultaneous gravitational attraction of several celestial bodies has been a goal. The straightforward solution of the two-body problem has always been used to roughly describe the motion of objects in space, but more accurate models are mandatory in most of the practical applications.

The Newton's equations of dynamics [1], developed in the XVII century, while not admitting an analytical solution, are able to estimate the motion of a mass-less particle under the simultaneous gravitational attraction of more than one massive body, by means of numerical integration. The absence of a closed form solution, and the attempt to derive more computationally efficient theories, have guided the search for models that were a compromise between accuracy and efficiency. The first attempt was the patched conics model [1], still adopted for first guess interplanetary trajectory design, that describes the particle motion as a series of Keplerian

orbits centred in the planet, whose gravitation attraction predominates on the others. This theory, while extremely computationally efficient, fails in providing accurate results whenever the celestial bodies exert a comparable force on the mass-less particle and, in any case, does not allow to predict the long-term evolution of orbits subjected to the third-body disturbance. In this scenario, more advanced theories were developed.

The Circular Restricted Three-Body Problem (CRTBP), despite limiting the analysis to just two celestial bodies, orbiting on circular orbits, retains the simultaneous and comparable effect of their gravity fields [2]. Moreover, the mathematical model has some peculiar features, namely equilibrium and periodic solutions and a constant of motion [2], which allow to have a first hint on the dynamics of a spacecraft subjected to the gravitational attraction of two celestial bodies.

The so-called perturbation approach, instead, faces the third-body disturbance as a perturbation that deviates the particle from the reference ideal Keplerian orbit [3]. The disturbing effect of a third body is usually modelled as a series expansion of the potential with respect to the ratio between the particle semi-major axis and the distance to the third body. In 1962, Cook formulated a theory to monitor the long-term fluctuations due to luni-solar perturbations [4]; he averaged the disturbing function after having expanded it up to the second term, considering circular orbit for the disturbing bodies. Kaufman (1972) [5] and Kaufman and Dasenbrock (1973) [6], included also higher order terms in the formulation. In more recent years, Colombo followed the same approach and added the double averaged formulation of the disturbing potential [7, 8].

In the middle of the two methods is the Keplerian map, that aimed at applying the perturbation approach to the three-body potential [9, 10]. The model was adopted by Ross and Scheeres [11] to monitor the effects of distant flybys in the planar CRTBP; to do so, they defined a semi-analytical energy kick function for non-parabolic orbits. After that, Alessi and Sànchez (2015) [12] and Neves et al. (2018) [13] developed semi-analytical formulations under the assumption of small mass parameter, applying the first Picard's iteration to the Lagrange planetary equations, to compute the orbital elements variations as kicks.

This paper investigates the physical model on which the Keplerian map relies; the formulation is extended to include the eccentric motion for the third body, as well as the hypothesis of small mass parameter is abandoned in favour of the exact form of the disturbing potential. The Lagrange planetary equations require the differentiation of the disturbing function with respect to the particle orbital elements, that is carried out coherently with the assumptions on which the equations of dynamics rely. The analysis includes an investigation about its accuracy and computational efficiency, that highlights the limits and potentialities, as well as the field of application, of the presented theory, opening to the possibility of exploiting the Keplerian map for trajectory design. A multi-flyby trajectory optimisation in the highly perturbed Jupiter sphere of influence (SOI) is finally proposed, using the Keplerian map as dynamical model.

2. Keplerian map theory

This section focuses on the theoretical formulation of the Keplerian map theory. Firstly, the exact form of the disturbing potential is derived, avoiding any assumption on the mass parameter μ of the binary system. The model is then extended to include the eccentric motion for the third body; hence, its position in space is defined according to an ephemeris model. Finally, the differentiation of the disturbing function with respect to the particle orbital elements is performed, according to the assumptions on which the Lagrangian brackets are derived [3].

2.1 The disturbing function

As mentioned, the Keplerian map theory applies the perturbation approach to the three-body potential. It is worth underlining that, adopting the Lagrange planetary equations as dynamical model, the reference trajectory must be described in terms of orbital elements. The gravitational potential of the three-body problem is defined with respect to the centre of mass, meaning that the orbital elements to be used are barycentric. As a matter of fact, the orbital elements refer to a planet located in the focus, which means that the unperturbed motion to take as reference is a fictitious physical system, with the primary located in the centre of mass, despite of the gravitational force exerted by the secondary body. This sub-section is devoted to demonstrating that the disturbing function can be obtained from the Newton's laws of dynamics, through the computation of the differential acceleration between unperturbed and perturbed motions, that coincide with those depicted in Figure 1, presented in a convenient spacecraft-oriented reference frame. This non-inertial reference frame follows the particle during its motion, such that it always lies on the xy plane.

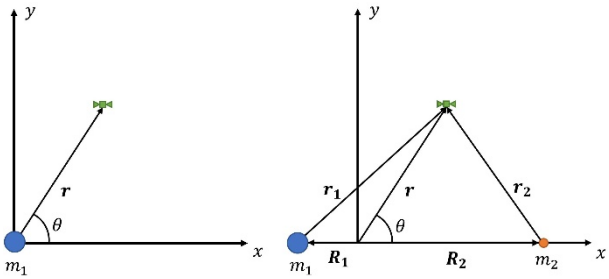

Figure 1: Unperturbed (left) and perturbed (right) models.

The proposed formulation is in dimensionless units: the sum of the masses of the two celestial bodies is equal to the identity and the mass parameter μ is defined as follows.

$$\mu = \frac{m_2}{m_1 + m_2} \tag{1}$$

where m_1 and m_2 are the masses of the primary and secondary bodies, respectively. Therefore, referring to Figure 1, the differential acceleration $\boldsymbol{\delta a}$ can be obtained, as follows.

$$\begin{aligned}\boldsymbol{\delta a} = &-\frac{1-\mu}{r_1^3}(\boldsymbol{r} - \boldsymbol{R_1}) - \frac{\mu}{r_2^3}(\boldsymbol{r} - \boldsymbol{R_2}) \\ &-\left(-\frac{1-\mu}{r^3}\boldsymbol{r}\right)\end{aligned} \tag{2}$$

where $\boldsymbol{r}$ is the particle position vector, $\boldsymbol{R_1}$ and $\boldsymbol{R_2}$ are the position vectors of the primary and secondary bodies with respect to the centre of mass. Since only conservative forces are involved, the differential acceleration of Eq. (2) can be written as gradient of a differential potential δU. Finally, the disturbing function R of the Keplerian map coincides with the differential potential δU, but changed in sign, as reported in Eq. (3).

$$R = -\left(-\frac{1-\mu}{r_1}\right) - \left(-\frac{\mu}{r_2}\right) + \left(-\frac{1-\mu}{r}\right) \tag{3}$$

where the minus signs are used to remark again the relation of the disturbing function with the gravitational potentials in brackets. The first two potentials are exerted on the particle by the primary and secondary bodies moving around the common centre of mass, while the third is the potential that would exert the primary if it were in the centre of mass, as in the fictitious unperturbed physical model.

2.2 Eccentric third body motion

The disturbing function of Eq. (3) is firstly transformed to be function of the mass-less particle and third body orbital radii and the time-varying angle θ, depicted in Figure 1. From the definition of system barycentre, the primary's position can be recovered, as follows.

$$R_1 = \frac{m_2}{m_1} R_2 = \frac{\mu}{1-\mu} R_2 \tag{4}$$

The distances r_1 and r_2 of the mass-less particle with respect to the primary and secondary bodies acquire the following form.

$$\begin{aligned} r_1 &= \sqrt{r^2 + \left(\frac{\mu}{1-\mu}\right)^2 R_2^2 + 2\frac{\mu}{1-\mu} r R_2 \cos\theta} \\ r_2 &= \sqrt{r^2 + R_2^2 - 2 r R_2 \cos\theta} \end{aligned} \tag{5}$$

The dependency of the disturbing function on the particle and third body orbital elements is now highlighted. The particle and third body orbital radii, referring to a formulation in true anomaly, can be written as:

$$\begin{aligned} r &= \frac{a(1-e^2)}{1 + e\cos\nu} \\ R_2 &= \frac{a_{3B}(1-e_{3B}^2)}{1 + e_{3B}\cos\nu_{3B}} \end{aligned} \tag{6}$$

The cosine of the angle θ can be computed taking the dot product between the normalized particle and third body position vectors, expressed in an inertial reference frame, through rotation matrices according to the Euler's angles, as follows.

$$\begin{aligned} \hat{\boldsymbol{r}}^{in} &= R_3(\Omega) R_1(i) R_3(\omega + \nu) \begin{Bmatrix} 1 \\ 0 \\ 0 \end{Bmatrix} \\ \widehat{\boldsymbol{R}}_2^{in} &= R_3(\Omega_{3\mathrm{B}}) R_1(i_{3B}) R_3(\omega_{3B} + \nu_{3B}) \begin{Bmatrix} 1 \\ 0 \\ 0 \end{Bmatrix} \end{aligned} \tag{7}$$

where R_j indicates the rotation matrix around axis j. Note that, since an ephemeris model is adopted for taking track of the position of third body over time, its orbital elements are updated inside the integration procedure. This is in contrast with previous authors' approach [12, 13], that, in the framework of the CRTBP, expressed the third body true anomaly as function of the particle one; unfortunately, when the hypothesis of circular orbit for the third body is abandoned, the relation true anomaly-time becomes non-linear also for the third body, causing this analytical relation impossible to be found.

2.3 Differentiation procedure

The disturbing function is differentiated with respect to the orbital elements, according to the Lagrange planetary equations [3]. It is worth underlining that the disturbing function to be adopted inside the Lagrange planetary equations must depend on six constant orbital elements and time, where constant means that under the hypothesis of Keplerian motion, they do not change with time. This fact affects the computation of the partial derivatives with respect to the orbital elements. Despite of its dependency on the true anomaly, the disturbing function must be thought as follows.

$$R = R\big(a, e, i, \Omega, \omega, \nu(M_0, t)\big) \tag{8}$$

where it is highlighted the dependency of the true anomaly on time and on the sixth constant orbital element M_0. The relations that link true anomaly and time are here recalled [1].

$$\begin{aligned} \nu &= 2\arctan\left(\sqrt{\frac{1+e}{1-e}}\tan\frac{E}{2}\right) \\ E - e\sin E &= nt + M_0 = \sqrt{\frac{1-\mu}{a^3}}t + M_0 \end{aligned} \tag{9}$$

Therefore, Eq. (8) can be written as:

$$R = R\big(a, e, i, \Omega, \omega, \nu(E(a, e, M_0, t), e)\big) \tag{10}$$

The orbital elements with respect to which the differentiation is performed are gathered in a vector $\boldsymbol{\alpha}$, as follows.

$$\alpha = [a \quad e \quad i \quad \Omega \quad \omega \quad M_0]^T \tag{11}$$

This allows to write the derivatives of the disturbing function with respect to vector $\boldsymbol{\alpha}$ of orbital elements in compact form, as follows.

$$\frac{dR}{d\boldsymbol{\alpha}} = \frac{\partial R}{\partial \boldsymbol{\alpha}} + \frac{\partial R}{\partial \nu}\frac{d\nu}{d\boldsymbol{\alpha}} \tag{12}$$

The derivatives of the true anomaly with respect to each element of vector $\boldsymbol{\alpha}$ can be expanded according to Eq. (10).

$$\begin{aligned} \frac{d\nu}{da} &= \frac{\partial \nu}{\partial E}\frac{\partial E}{\partial a} \\ \frac{d\nu}{de} &= \frac{\partial \nu}{\partial e} + \frac{\partial \nu}{\partial E}\frac{\partial E}{\partial e} \\ \frac{d\nu}{dM_0} &= \frac{\partial \nu}{\partial E}\frac{\partial E}{\partial M_0} \end{aligned} \tag{13}$$

where:

$$\begin{aligned} \frac{\partial \nu}{\partial E} &= \frac{1 + e\cos\nu}{\sqrt{1-e^2}} \\ \frac{\partial E}{\partial a} &= -\frac{3}{2a}\frac{E - e\sin E - M_0}{1 - e\cos E} \\ \frac{\partial \nu}{\partial e} &= \frac{\sin\nu}{1-e^2} \end{aligned} \tag{14}$$

$$\begin{aligned} \frac{\partial E}{\partial e} &= \frac{\sin\nu}{\sqrt{1-e^2}} \\ \frac{\partial E}{\partial M_0} &= \frac{1 + e\cos\nu}{1-e^2} \end{aligned}$$

3. Model validation

This section is devoted to the validation of the Keplerian map theory derived in Section 2. In the first part, the model will be adopted to propagate several times the orbit of a Near-Earth asteroid, characterised by relatively high uncertainty on its orbital elements, to test a very wide range of conditions. This first analysis is intended to verify both the accuracy and the computational efficiency of the proposed algorithm. In the second part, the propagation of the JUICE spacecraft orbit will be of interest; since the four Galilean moons all exert a non-negligible force inside the sphere of influence of the gaseous planet, this is an ideal application to test the many-body scenario.

3.1 Near-Earth asteroid close encounters

The Near-Earth Object (NEO) selected for this analysis is 2010 JL88, classified as Apollo asteroid. Apart from the high uncertainty on its actual position and velocity, it guarantees to test the Keplerian map when very close to the disturbing body, since the predicted minimum close approach falls well inside the Earth spere of influence. The orbital elements of the target asteroid at epoch 31/05/2020 are reported in Table 1.

Table 1: Asteroid 2010 JL88 orbital elements at epoch 31/05/2020 (heliocentric ecliptic J2000), JPL Small-Body Database Browser [14].

Elements	Value	Uncertainty
a [AU]	1.423101860964695	0.00044663
e [−]	0.5033962990156285	0.00023077
i [deg]	0.09381670240039022	0.003563
Ω [deg]	268.6297439926558	0.35215
ω [deg]	51.55100438911916	0.35382
M [deg]	0.5033962990156285	0.00044663

The nominal and minimum closest approach distances are predicted by JPL to happen at 0.02678 AU and 0.00118 AU from the Earth surface at epoch 05/11/2020 [14] respectively, to be compared with the Earth sphere of influence of 0.00618 AU.

The comparison is carried out as follows:

- The nominal set of orbital elements is propagated for one asteroid orbital period by means of the Keplerian map and of numerical propagation of Newton's laws of dynamics [1]; The resulting profiles are compared.

- The same propagation is held several times, extracting the orbital elements from Gaussian distributions based on the nominal values and uncertainties of Table 1.
- An accuracy and computational costs analysis is performed on the basis of the results obtained.

In Figure 2, the profiles resulting from the propagation of the nominal Keplerian elements are presented.

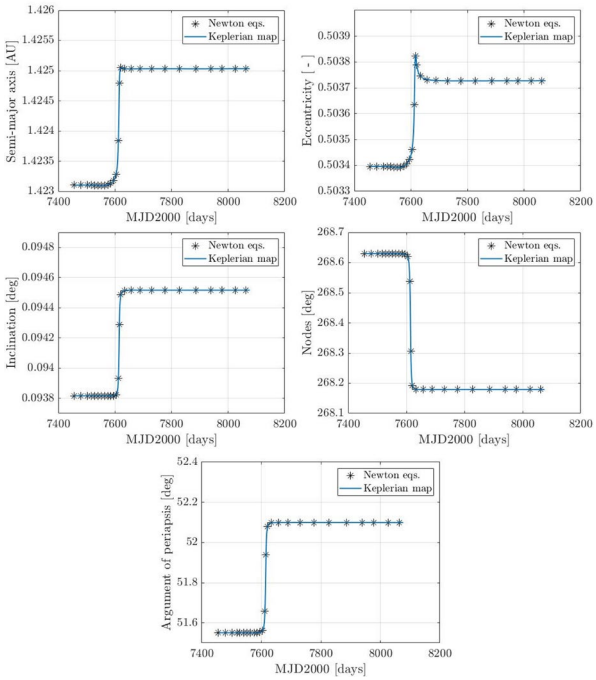

Figure 2: Asteroid 2010 JL88 nominal Keplerian elements propagation, one orbital period.

As it can be observed, the Keplerian map allows to predict exactly the orbital elements variations, as the profiles overlap with the reference ones. The predicted nominal closest approach distance from the Earth is 0.02683 AU, very close to the actual one, despite of the missing perturbation models.
The second analysis is now of interest; the accuracy of the model is assessed monitoring the error in terms of semi-major axis value at the end of the one orbital period propagation, as follows.

$$\text{Rel. err.}_{\%} = \frac{|\Delta a_{\text{KM}} - \Delta a_{\text{Newton}}|}{|\Delta a_{\text{Newton}}|} \cdot 100 \qquad (15)$$

$$\text{Abs. err.} = |\Delta a_{\text{KM}} - \Delta a_{\text{Newton}}|$$

One thousand samples from the Gaussian distributions have been considered; in Figure 3 are reported the errors and the corresponding values of the semi-major axis variation.

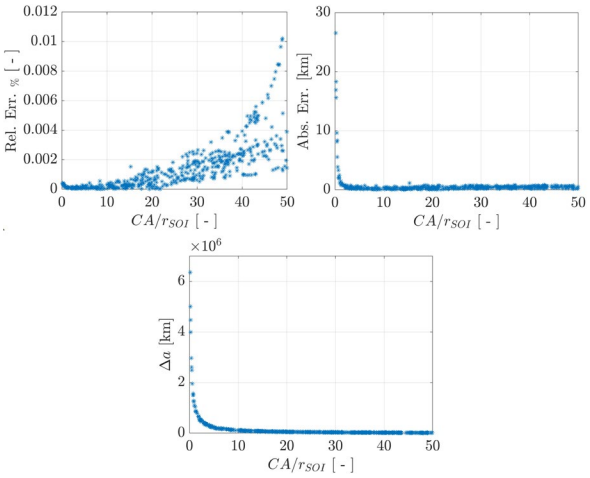

Figure 3: Accuracy analysis results - Keplerian map error as function of Earth distance.

As it can be observed, the error remains extremely low independently of the third body distance. It is worth noticing that the trend of increasing relative error at high distance from the Earth is not related to a reduced ability of the model; on the contrary, this tendency comes as a consequence of the lower effects of the Earth in distorting the asteroid trajectory, whose orbital elements undergo negligible variations during one revolution. As a result, the relative error grows as the denominator tends to zero. The computational efficiency analysis is performed comparing the time required by the two models for the one thousand asteroid orbital motion computations of the accuracy analysis, as well as the average number of time steps and function evaluations needed by the numerical integrator. The results are presented in Table 2.

Table 2: Results of the computational efficiency analysis. Processor: Intel(R) Core(TM) i7-10700 CPU @ 2.90 GHz, ODE solver: `ode45` Matlab® R2020b.

	Newton eqs.	**Keplerian map**
CPU time [s]	38.5	33.5
n° of time steps	479	170
n° of fun. evals.	1208	286

The Keplerian map theory was able to reduce the time needed by almost the 17%. This gain is relatively low if compared with the average number of steps and function evaluations, which are approximately 2.8 and 4.2 times lower. This is caused by the more complex dynamics equations of the Keplerian map; as a result, the slow-varying dynamics based on Keplerian elements can be only partially exploited, since the evaluation of the derivatives of the disturbing function with respect to the orbital elements requires a relatively long time. Nevertheless, the proposed model remains more efficient with respect to the classical formulation in Cartesian coordinates. This gain could be an advantageous

opportunity in case of large trajectory optimisation problems of real applications.

3.2 JUICE spacecraft orbit propagation

The JUpiter ICy moons Explorer (JUICE) is the first large-class mission in ESA's Cosmic Vision 2015-2025 programme. Planned for launch in May 2022 and arrival at Jupiter in October 2029, it will spend at least three years making detailed observations of the giant gaseous planet Jupiter and three of its largest moons, Ganymede, Callisto and Europa. Because of the four massive moons that orbit around Jupiter, the spacecraft motion is affected by their gravitational attraction. For this reason, this turns out to be the best scenario for checking the accuracy of the Keplerian map when many celestial bodies simultaneously exert a non-negligible gravitational force on a spacecraft. In the Jupiter system, at least two other perturbations are comparable in magnitude to the moons gravitational disturbance, namely the Sun gravitational potential and Jupiter zonal harmonics. Their effect will be accounted in the analysis. The Sun gravitational potential is included adopting the perturbation approach with single averaged disturbing function [8], because the spacecraft distance from Jupiter is much smaller than its distance from the Sun. The Jupiter zonal harmonics effect is modelled by means of the classical theory based on Legendre polynomials [3].

The comparison presented in the following is limited to a relatively short phase of the mission, planned between 10/02/2031 and 25/04/2031, when the JUICE spacecraft remains outside the moons' sphere of influence. Indeed, even though the Keplerian map works efficiently even when very close to the disturbing body, a very precise model of the other perturbations is not included, since it is not the goal of this study. Hence, a proper estimate of the effect of a flyby would not be possible, since these manoeuvres are extremely sensitive to small variations of the approaching trajectory. Furthermore, the orbital manoeuvres performed by the probe are not modelled, which means that the estimated profiles would diverge from the ephemeris in any case.

In Figure 4 are reported the results of the comparison in terms of orbital elements profiles. The perturbations previously mentioned are added once at a time, to observe their effects on the spacecraft motion. Note that the prediction given by the integration of the Newton's equations is included as well, to assess the accuracy of the Keplerian map in the many-body scenario.

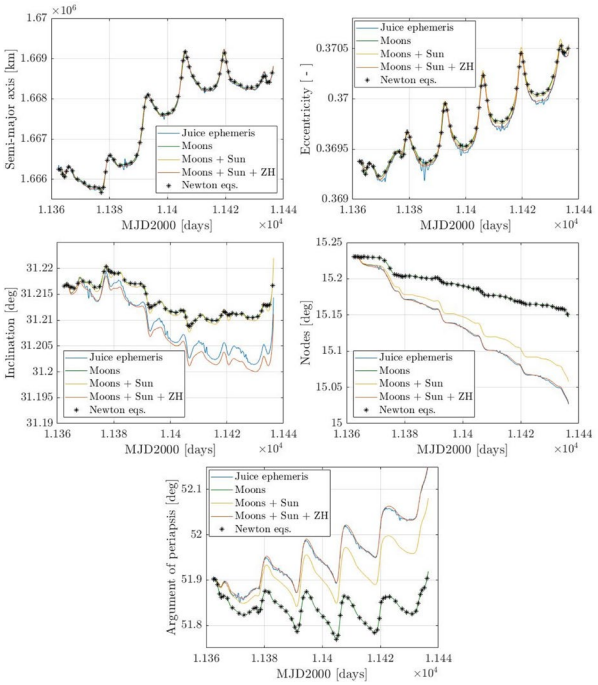

Figure 4: JUICE orbital elements profiles, 10/02/2031 - 25/04/2031.

As it can be observed, the estimates given by just the application of the Keplerian map, to model the gravitational disturbance of the Galilean moons, are exact, as they overlap with the propagations of the Newton's equations. Adding the two additional perturbative effects, the orbital elements profiles approach the actual ephemeris of the JUICE spacecraft; the residual error, more evident in the inclination profile, derives from other perturbative effects that were not included in the model.

4. Multi-flyby trajectory design around Jupiter

The design of a trajectory typically involves large optimisation processes, in which potential trajectories are computed several times by the routine adopted. Therefore, the computational efficiency of the Keplerian map can be exploited to ease the search for the optimal solution of the needed transfer. As already mentioned, the gravitational field in the Jupiter sphere of influence is highly distorted by the four Galilean moons; as a result, the design of a mission around the giant planet must account for the effects the moons have on the spacecraft dynamics. The proposed study aims at designing a multi-flyby trajectory, accounting for the simultaneous and continuous attraction of Jupiter and the massive moons. The design of multi-flyby trajectories is a complex task due to the size of the problem to be optimised; therefore, at the first instance, it is convenient to simplify the model as much as possible, to obtain a first guess solution that will be refined in second analysis. Therefore, the patched conics approximation [1] is adopted just as first guess solution generator, whose output is submitted to a second

optimisation algorithm, that accounts for the gravitational disturbance of the moons along the whole spacecraft path. Since the JUICE spacecraft is planned to perform several flybys around Callisto, Ganymede and Europa, its trajectory is taken as reference to define the initial and target orbits for the optimisation. The phase considered is foreseen between 01/2030 and 09/2030, when, after the capture, the altitude is lowered before beginning the scientific phase of the mission. The orbital elements of the initial and target orbits are listed in Table 2.

Table 3: Orbital elements of initial and target orbits.

Elements	Initial	Target
a [km]	$1.0286 \cdot 10^7$	$1.7389 \cdot 10^6$
e [−]	0.9207	0.6108
i [deg]	3.6622	1.6659
Ω [deg]	265.0557	331.5952
ω [deg]	189.1088	114.1121

4.1 Patched conics-based optimisation

The genetic algorithm routine is exploited to generate a first guess trajectory, whose output are the departure, flybys and arrival times, and the sequence of moons to be flown. At this stage, the figure of merit is the total cost of the mission, detailed in Eq. (16).

$$\Delta v_{tot} = \left\|\boldsymbol{v}_L^i - \boldsymbol{v}_{dep}\right\| + \sum_{j=1}^{N_{\text{fb}}} \Delta v_{\text{fb}}^j + \left\|\boldsymbol{v}_{arr} - \boldsymbol{v}_L^f\right\| \quad (16)$$

where $\boldsymbol{v}_L^i$ is the initial velocity on the first Lambert arc, $\boldsymbol{v}_{dep}$ is the velocity on the departure orbit at the time when the first manoeuvre is given, Δv_{fb}^j are the manoeuvres to be given at the hyperbolas periapsis to link the incoming and outgoing trajectories, $\boldsymbol{v}_{arr}$ is the velocity on the final orbit when the latter is reached and $\boldsymbol{v}_L^f$ is the final velocity on the last Lambert arc.

4.2 Keplerian map-based optimisation

The aim of this second optimisation algorithm is to refine the trajectory, abandoning the assumptions of the patched conics model; the general idea is here summarized:

- The ideal trajectory is divided into a number of phases equal to the number of Lambert arcs designed.
- Each phase is divided in two sub-phases at the connection of which a deep space manoeuvre is given.
- Each manoeuvre (departure, hyperbola perigee burns, arrival and deep space manoeuvres) is optimised to get the aimed continuous path that brings the spacecraft from the initial to the final orbit, accounting for the gravitational disturbances of all the Jovian moons, through the Keplerian map.

This second optimisation stage relies on a double shooting algorithm; to explain in detail the way it works, the hypothetical double flyby trajectory schematised in Figure 5 is considered.

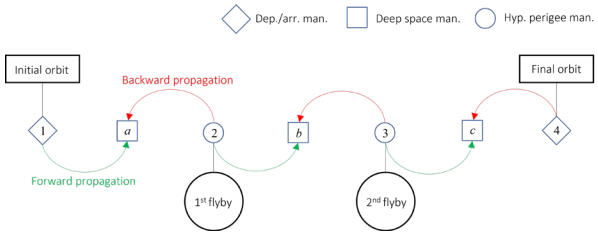

Figure 5: Shooting method scheme.

Arc 1-2. During the first phase, the algorithm is constrained by the following quantities:

- t_1: departure time, when the first manoeuvre is given.
- t_2: first flyby time, as designed by the patched conics-based optimisation process.
- $[\boldsymbol{r}_1, \boldsymbol{v}_1]$: initial spacecraft state vector, before the departure manoeuvre.
- $[\boldsymbol{r}_2, \boldsymbol{v}_2]$: spacecraft state vector at the perigee of the first hyperbola, before hyperbola perigee burn, as computed by the patched conics-based optimisation process.

The double shooting method, that relies on the constrained function minimization routine, aims at finding the optimal departure manoeuvre vector $\Delta\boldsymbol{v}_{dep}$ and deep space manoeuvre time t_a, according to the following steps:

a. The spacecraft state vector after the departure manoeuvre is computed, as follows.

$$[\boldsymbol{r}_1, \boldsymbol{v}_1^+] = [\boldsymbol{r}_1, \boldsymbol{v}_1 + \boldsymbol{\Delta v}_{dep}] \quad (17)$$

b. The state vector of Eq. (17) is converted into orbital elements and propagated forward, with the Keplerian map algorithm, up to the deep space manoeuvre time t_a.

c. The final spacecraft state vector $[\boldsymbol{r}_2, \boldsymbol{v}_2]$ is converted into orbital elements, as well, and propagated backward from t_2 to t_a.

d. The quantity to be minimised is the cost function here reported:

$$J = \left\|\boldsymbol{r}_{fp}^f - \boldsymbol{r}_{bp}^f\right\| + \alpha\left(\left\|\boldsymbol{v}_{fp}^f - \boldsymbol{v}_{bp}^f\right\| + \Delta v_{dep}\right) \quad (18)$$

Where $\boldsymbol{r}_{fp}^f$ and $\boldsymbol{v}_{fp}^f$, $\boldsymbol{r}_{bp}^f$ and $\boldsymbol{v}_{bp}^f$ are the position and velocity vectors at the end of the forward and

backward propagations, respectively, and α is a factor to weight the relative importance of the two terms. Note that the term in brackets on the right-hand side is the total cost of the first phase.

e. The difference in spacecraft velocity at the end of forward and backward propagations defines the deep space manoeuvre:

$$\boldsymbol{\Delta v}_a = \boldsymbol{v}_{fp}^f - \boldsymbol{v}_{bp}^f \tag{19}$$

It is important to make a note on the factor α of Eq. (18). It must be kept in mind that, until the two position vectors do not coincide, the computed deep space manoeuvre is meaningless. It is therefore reasonable to give more importance to the difference in position rather than velocity. Since an error in position below one hundred kilometres provokes just a small error in the final states and knowing that the total cost of the phase is of the order of the unit, or below, a first reasonable guess value of the factor α is 10^2. Note that this value could be refined according to the characteristics of the arc to be optimised. Before proceeding with the second arc, the first arc is computed on the basis of the defined parameters; indeed, even though the optimisation function ensures that the hyperbola perigee is reached, small errors in the matching point could cause a slight deviation in the final states and the epoch at which the hyperbola perigee is reached. The final states $[\boldsymbol{r}_2^*, \boldsymbol{v}_2^*]$ and final time t_2^* of the propagation are the input for the second arc.

Arc 2-3. During the second phase, the algorithm is constrained by the following quantities:

- t_2^* : first flyby time, output of the first arc optimisation.
- t_3: second flyby time, as designed by the patched conics-based optimisation process.
- $[\boldsymbol{r}_2^*, \boldsymbol{v}_2^*]$: spacecraft state vector at the perigee of the first hyperbola, before the hyperbola perigee burn, output of the first arc optimisation.
- $[\boldsymbol{r}_3, \boldsymbol{v}_3]$: spacecraft state vector at the perigee of the second hyperbola, after the hyperbola perigee burn, as designed by the patched conics-based optimisation process.

In the flyby-to-flyby phase, the double shooting method aims at finding the optimal hyperbolas perigee manoeuvres $\boldsymbol{\Delta v}_{fb}^2$ and $\boldsymbol{\Delta v}_{fb}^3$ and the deep space manoeuvre time t_b, according to the following steps:

a. The spacecraft state vector after the first hyperbola perigee burn is computed, as follows.

$$[\boldsymbol{r}_2^*, \boldsymbol{v}_2^+] = [\boldsymbol{r}_2^*, \boldsymbol{v}_2^* + \boldsymbol{\Delta v}_{fb}^2] \tag{20}$$

After the Cartesian to Keplerian coordinates transformation, the orbital elements are propagated forward up to the deep space manoeuvre time t_b, by means of the Keplerian map algorithm.

b. The spacecraft state vector, before the second hyperbola perigee burn, is computed according to the following relation:

$$[\boldsymbol{r}_3, \boldsymbol{v}_3^-] = [\boldsymbol{r}_3, \boldsymbol{v}_3 - \boldsymbol{\Delta v}_{fb}^3] \tag{21}$$

After the usual Cartesian to Keplerian coordinates transformation, the orbital elements are propagated backward up to the deep space manoeuvre time t_b.

c. For the second arc, the cost function modifies as follows.

$$J = \left\|\boldsymbol{r}_{fp}^f - \boldsymbol{r}_{bp}^f\right\| + \alpha\left(\left\|\boldsymbol{v}_{fp}^f - \boldsymbol{v}_{bp}^f\right\| + \Delta v_{fb}^2 + \Delta v_{fb}^3\right)$$

where, again, the term in brackets is the total cost of the second phase.

As it has been done for the first arc, the second arc is computed before proceeding with the optimisation of the last arc. This latter is optimised in the same way, with the arrival manoeuvre $\boldsymbol{\Delta v}_{arr}$ and last deep space manoeuvre time t_c as variables.

4.3 Results of the trajectory optimisation

The trajectory optimisation process led to a two-flyby strategy, with the close approaches happening on Callisto and Ganymede at a perigee altitude of 2950 km and 254 km, respectively; the trajectory is depicted in Figure 6 and summarized in Table 3 and Table 4 in terms of numerical results.

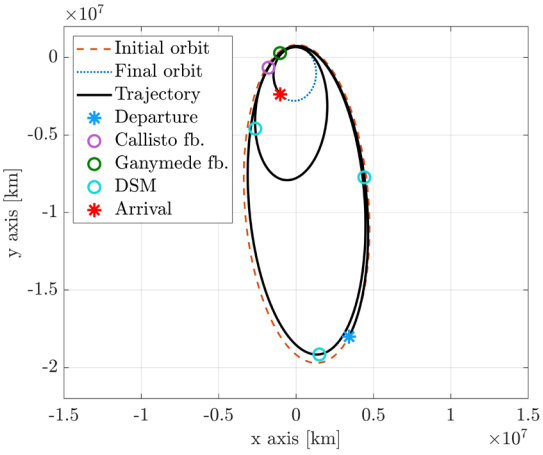

Figure 6: Optimal trajectory.

Table 4: Mission timeline – Comparison between first and second stages of optimisation.

Dates	Patched conics	Double shoot.
Departure	26/02/2030	26/02/2030
DSM_1	-	21/04/2030
Callisto fb.	10/05/2030	10/05/2030
DSM_2	-	19/08/2030
Ganymede fb.	28/11/2030	28/11/2030
DSM_3	-	08/12/2030
Arrival	24/01/2031	24/01/2031
TOF [dd]	332	332

Table 5: Mission costs – Comparison between first and second stages of optimisation.

Δv [m/s]	Patched conics	Double shoot.
Departure	53.7	60.2
DSM_1	-	13.9
Callisto fb.	0.1	8.2
DSM_2	-	24.6
Ganymede fb.	0.01	24.9
DSM_3	-	14.6
Arrival	1209.3	1216.5
TOT	1263.1	1362.9

As it can be observed by looking at the manoeuvres' cost reported in Table 4, the total cost of the mission increased by only 8 % to counteract the gravitational disturbance caused by the Galilean moons during the spacecraft cruise. It is worth mentioning that a higher number of deep space manoeuvres would probably lead to a further refinement of the result, as it would add more flexibility. To conclude, in Figure 7 are depicted the profiles of the Keplerian elements during the whole mission. As it can be noticed, the first flyby on Callisto mainly varies the Euler's angles of the spacecraft orbit, making them more similar to the ones of the target orbit. On the other hand, the second flyby on Ganymede strongly reduces the semi-major axis and eccentricity, which are then further lowered by the arrival impulsive manoeuvre.

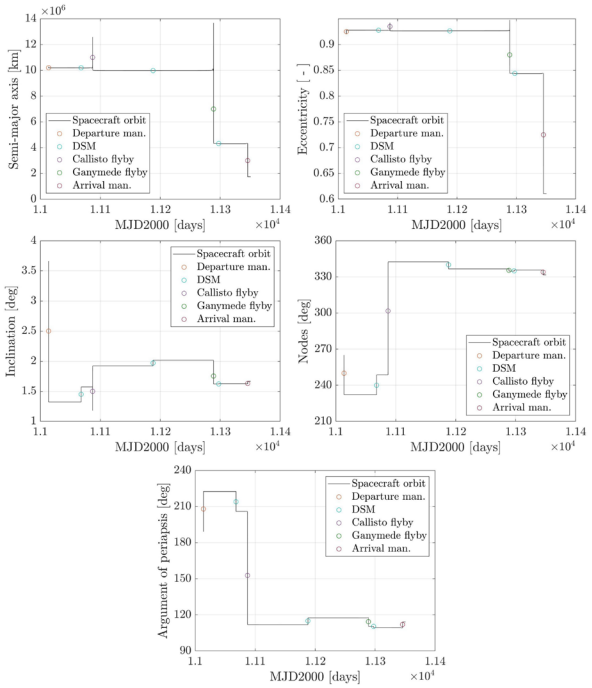

Figure 7: Orbital elements profiles.

5. Conclusions

The Keplerian map theory proposed in this paper aimed at accurately modelling the motion of a mass-less particle under the simultaneous gravitational attraction of many celestial bodies. To accomplish this objective, some fundamental modifications have been introduced with respect to the existing formulations. In particular, the disturbing function was computed without including any assumption on the mass-parameter of the binary system, which potentially extends the field of application of the model to any binary system. The motion of the disturbing bodies was included based on an ephemeris model, abandoning the hypothesis of circular motion. Finally, the accounted dependency of the disturbing function on the independent variable (i.e., time), according to the requirement of the Lagrange planetary equations, had an enormous beneficial effect on the accuracy of the Keplerian map theory. These improvements dramatically extended the field of application of the model, which proved its validity in different orbital regimes; in particular, the propagation of the orbit of the JUICE spacecraft highlighted the capabilities of the Keplerian map in the many-body scenario. Furthermore, the theory demonstrated to be very efficient from a computational point of view, if compared with the classical formulation in Cartesian coordinates. The good results of the model validation analysis opened the doors to its use in large trajectory optimisation problems. This paper successfully proposed the design of a multi-flyby trajectory in the sphere of influence of Jupiter, under the simultaneous attraction of all the Galilean moons.

Acknowledgements

This project has received funding from the European Research Council (ERC) under the European Union's Horizon 2020 research and innovation programme (grant agreement No 679086 - COMPASS).

References

[1] Vallado, D.A., *Foundamental of astrodynamics and applications*, 1st ed., McGraw-Hill, 1997.

[2] Roy, A.E., *Orbital motion*, 4th ed., Institute of Physics Publishing, 2005.

[3] Battin, R.H., *An Introduction to the Mathematics and Methods of Astrodynamics*, 1st ed., AIAA, 1999.

[4] Cook, G.E., "Luni-Solar Perturbations of the Orbit of an Earth Satellite," *Geophysical Journal International*, Vol. 6, pp. 271-291, 1962.

[5] Kaufman, B., *Higher Order Theory for Long-Term Behaviour of Earth and Lunar Orbiters*, NRL Report 7527, Naval Research Laboratory, 1972.

[6] Kaufman, B., Dasenbrock, R., "Semianalytic Theory of Long-Term Behavior of Earth and Lunar Orbiters," *AAIA/AAS Astrodynamics Conference*, Vol. 10, 1973.

[7] Colombo, C., "Long-term evolution of highly-elliptical orbits: luni-solar perturbation effects for stability and re-entry," *Proceedings of the 25th AAS/AIAA Space Flight Mechanics Meeting*, pp. 3117-3140, 2015.

[8] Colombo, C., "Long-Term Evolution of Highly-Elliptical Orbits: Luni-Solar Perturbation Effects for Stability and Re-entry," *Frontiers in Astronomy and Space Sciences*, Vol. 6, pp. 34, 2019.

[9] Petrosky, T.Y., and Broucke, R., "Area-Preserving Mappings and Deterministic Chaos for Nearly Parabolic Motion," *Celestial Mechanics*, Vol. 42, pp. 53-79, 1988.

[10] Chirikov, B.V., and Vecheslavov, V.V., "Chaotic Dynamics of Comet Halley," *Astronomy and Astrophysics*, 1989.

[11] Ross, S., and Scheeres, D.J., "Multiple gravity assists in the Restricted Three-Body Problem," *SIAM Journal on Applied Dynamics Systems*, Vol. 6, pp. 576.596, 2007.

[12] Alessi, E.M., and Sànchez, J.P., "Semi-Analytical Approach for Distant Encounters in the Spatial Circular Restricted Three-Body Problem," *Journal of Guidance, Control, and Dynamics*, 2015.

[13] Neves, R., Sànchez, J.P., Colombo, C., and Alessi, E.M., "Analytical and Semi-Analytical Approaches to the Third-Body Perturbation in Nearly Co-Orbital Regimes," *69th International Astronautical Congress*, 2018.

[14] https://ssd.jpl.nasa.gov/sbdb.cgi?sstr=2010\%20JL88. Last accessed 19/11/2020.